

Bonding nature of metal/oxide incoherent interfaces by first-principles calculationsKatsuyuki Matsunaga,^{1,*} Takeo Sasaki,² Naoya Shibata,³ Teruyasu Mizoguchi,³ Takahisa Yamamoto,⁴ and Yuichi Ikuhara³¹*Department of Materials Science and Engineering, Kyoto University, Yoshida-honmachi, Sakyo-ku, Kyoto 606-8501, Japan*²*Department of Materials Engineering, The University of Tokyo, 2-11-16, Yayoi, Bunkyo-ku, Tokyo 113-8656, Japan*³*Institute of Engineering Innovation, The University of Tokyo, 2-11-16, Yayoi, Bunkyo-ku, Tokyo 113-8656, Japan*⁴*Department of Advanced Materials Science, Graduate School of Frontier Science, The University of Tokyo, 5-1-5, Kashiwanoha, Kashiwa-shi, Chiba 227-8561, Japan*

(Received 23 May 2006; revised manuscript received 23 July 2006; published 27 September 2006)

A bonding mechanism of large-mismatched metal/oxide heterointerfaces, classified as incoherent interfaces, is investigated by first-principles calculations. As a model system, incoherent Ni/ZrO₂(111) interfaces are selected, and the interfacial bonding characters and their relevance to the interface strength are analyzed. It is found that the chemical bonds of the interfacial atomic pairs are strongly dependent on the atomic configurations in the interface structures, and show a site-dependent character from ionic through covalent/metallic bonding. Thus, even in the presence of a large misfit, stable interfaces can be formed by an effective chemical bonding transition along the interfaces. First-principles tensile tests show that such a bonding multiplicity strongly affects the atomic-scale fracture behavior and ideal mechanical strength of the interfaces.

DOI: [10.1103/PhysRevB.74.125423](https://doi.org/10.1103/PhysRevB.74.125423)

PACS number(s): 73.20.-r, 73.43.Cd

Heterointerfaces are important components in microstructures of advanced materials such as composites and coatings, and their interfacial properties often determine overall performance and reliability of the materials systems. Among heterointerfaces, combination of metal and metal-oxide has been extensively studied experimentally and theoretically,^{1,2} in order to obtain detailed knowledge on bonding characteristics across the interfaces. However, the interfacial bonding is generally difficult to describe simply by a particular chemical bonding state such as metallic or ionic, because the two constituent materials have dissimilar electronic structures. Moreover, differences in crystal structures and lattice parameters may also affect the interfacial bonding state. Therefore, it is essential to reveal a generic and detailed bonding mechanism of metal/oxide interfaces.

From a theoretical viewpoint, a number of metal/oxide interface systems have been studied by the first-principles method, together with a supercell approach.¹⁻⁸ However, although most of real metal/oxide interfaces contain lattice misfits, previous theoretical calculations dealt with specific coherent interface models without lattice misfits. In this case, several symmetric coherent structures (all metal atoms are located at certain symmetric sites on an oxide surface) were assumed in supercells. As a matter of course, coherent interface models contain a particular type of interfacial atomic-pair configuration such as on top, hollow, and bridging, and thus the bonding state over the interface plane can also be understood by its particular character of bonding.

In contrast, real metal/oxide interfaces with lattice misfits undergo misfit strains, and the strains are relaxed in a semicoherent or incoherent manner. In the semicoherent case (typically, several percent of lattice misfit), it is known that a two-dimensional network of misfit dislocations is introduced to accommodate the misfit strain, and the interface areas between misfit dislocations can be regarded as coherent structures. Based on this situation, Hong *et al.* performed coherent-model calculations of Ag/MgO(100) interfaces, which is semicoherent in reality, and the calculated proper-

ties were corrected by the energy of misfit dislocations.³ More recently, Benedek *et al.* calculated the semicoherent Cu/MgO{222} oxygen-terminated interface, and showed that the interface properties can be represented by average of interface properties for different symmetric coherent structures.⁹

On the other hand, when a lattice misfit of a metal/oxide interface exceeds 10% or more, the interface structure cannot be described by arrays of misfit dislocations as found in semicoherent interfaces.¹⁰ In this case, unlike in coherent or semicoherent interfaces, long-range lattice continuity across the interface is missing, and the interface structure is referred to as incoherent. Originally, a truly incoherent interface implies a complete lack of lattice continuity and bonding across an interface plane, and thus adhesion of metal and oxide cannot be realized.¹¹ However, a number of interfaces such as Cu(111)/Al₂O₃(0001) and Ni(111)/YSZ(111) were experimentally found to form incoherent structures.¹²⁻¹⁵ The real incoherent interfaces exhibit specific orientation relationships and adhesion, which is evidence for the presence of particular interfacial bonding states. Due to worse lattice continuity of incoherent interfaces compared to coherent or semicoherent ones, various kinds of metal-cation or metal-oxygen bonding pairs in on-top, hollow, and bridging configurations and so forth coexist and play an important role for interface adhesion. In order to understand properties of incoherent metal/oxide interfaces, such characteristic bond configurations across the interface plane should be taken into account.

Bonding and adhesion properties of large-mismatched metal/oxide interfaces were often explained qualitatively by differences in lattice parameters and elastic constants between metal and oxide lattices.^{2,11,16,17} Also, the image charge theory^{1,2} is used to qualitatively understand the interfacial bonding, but the above arguments do not explicitly take account of detailed interfacial atomic configurations and their bonding states. Moreover, as stated above, most of previous first-principles studies on metal/oxide interfaces are

limited to coherent cases, and thus the physical origin of adhesion in incoherent metal/oxide interfaces is poorly understood so far.

In this study, bonding characteristics and the associated mechanical properties of incoherent metal/oxide interfaces are investigated in a first-principles manner. In interface modeling for theoretical calculations, it is important to use supercells appropriate for incoherent metal/oxide interfaces. For this purpose, the coincidence boundary model is used here, which assumes that, even in an incoherent interface, an interface-energy minimum will occur when a fraction of interfacial atoms in a softer crystal lattice are slightly relaxed and occupy specific coincidence positions on a stiffer crystal surface.¹⁸ A large-mismatched metal/oxide interface can now be described by a basic unit whose length parallel to the interface plane is $ma_o^0 \approx na_m^0$, where m and n are integers, and a_o^0 and a_m^0 are unit lengths of oxide-lattice and metal-lattice planes perpendicular to an interface, respectively. A misfit parameter δ in this case is defined by $\delta = (ma_o^0 - na_m^0)/na_m^0$. Therefore, it is necessary to select an incoherent metal/oxide system for which first-principles calculations are feasible and in which the δ value can be minimized as small as possible, using smaller integers of m and n .

Based on the above requirement for supercell modeling, a number of metal/oxide interfaces studied experimentally so far were reviewed, and eventually the interface system of Ni(111)/ZrO₂(111) is selected as an optimum incoherent model of this study. In our previous report, the experimental high-resolution transmission electron microscopy (HRTEM) image of the Ni/cubic yttria-stabilized ZrO₂ (YSZ) interface showed that this interface having a lattice misfit of 31% is atomically sharp with a cube-on-cube orientation relationship (OR) of $(111)_{\text{Ni}} \parallel (111)_{\text{YSZ}}$ and $[1\bar{1}0]_{\text{Ni}} \parallel [1\bar{1}0]_{\text{YSZ}}$, and no misfit dislocations are observed along the interface plane, indicating the incoherent structure.¹⁵ For this incoherent system, a misfit-free condition of $\delta=0$ in the coincidence boundary model cannot be attained even for large m and n values, but a coincidence repeat unit with a rather small misfit of $\delta=-2.7\%$ can be obtained by using relatively small integers of $m=2$ and $n=3$ along the $\langle 1\bar{1}0 \rangle$ direction. Accordingly, repeat units of ZrO₂(111) and Ni(111) parallel to the interface plane are extended by 2×2 and 3×3 along $\langle 1\bar{1}0 \rangle$, respectively, in the supercell construction. Supercell configurations viewed normal to the interface plane are displayed in Fig. 1. The remaining misfit of $\delta=-2.7\%$ is compensated by compressing the Ni slabs parallel to the interface plane, because the ZrO₂ lattice is stiffer than the Ni lattice. It can be said that the original lattice misfit between Ni and ZrO₂ (31%) can be minimized up to 2.7% by using the extended interface supercell.

Even for the extended supercell of the interface, there are a number of possible interface configurations with respect to relative translation states between Ni and ZrO₂ lattices. In reality, it is reasonable to describe the incoherent structure by a mixture of different translation states. In the present interface model, the interface configuration can be repeated by a translation vector of $\mathbf{t} = a_{\text{ZrO}_2}/3[\bar{2}11]$, and two different translation states of T_0 and T_1 are considered as representative

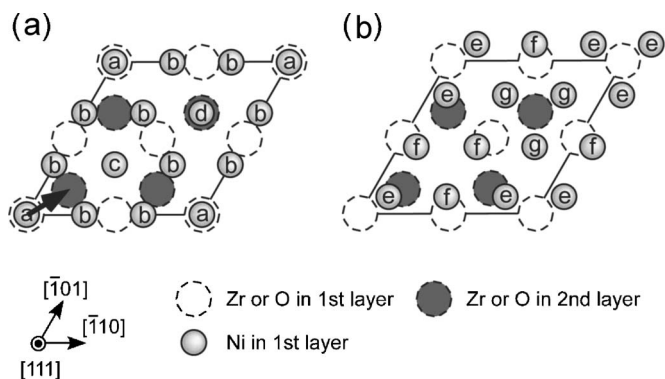


FIG. 1. Atomic arrangement of the interface supercells, projected on the interface plane. (a) the translation state of T_0 and (b) of T_1 . In this figure, one Ni layer and two ZrO₂ layers adjacent to the interface are only shown. The arrow in (a) indicates a minimum translation vector of $\mathbf{t} = a_{\text{ZrO}_2}/3[\bar{2}11]$. In each model, Ni atoms located at equivalent sites on the ZrO₂ surface are assigned by using alphabetical characters from “a” to “g.”

translated structures, where the T_1 structure is obtained by a translation of $2\mathbf{t}/3$ from T_0 . The atomic positions of Ni in T_0 can be represented by four kinds of positions on ZrO₂ (111) [$a-d$ in Fig. 1(a)]; an on-top site (a), an asymmetric site slightly off from the on-top location (b) and two kinds of hollow sites c and d (the d site is atop an atom in the second ZrO₂ layer). In contrast, the atomic configurations across the interface plane in T_1 are quite different from those in T_0 , where Ni atoms are situated at three kinds of asymmetric positions on the ZrO₂ surface [$e-g$ in Fig. 1(b)].

Each interface supercell comprises a ZrO₂(111) slab sandwiched by Ni(111) slabs. Since $\{111\}$ planes of c -ZrO₂ are polar planes composed of Zr or O atoms, Zr and O terminated interfaces are considered in this study. In order to avoid spurious effects of dipole moments on atomic structures and energies of the slab models, the Zr and O terminated ZrO₂ slabs have identical surface termination, and then contain ten and nine ZrO₂ (111) layers, respectively. It is noted that the O terminated slab is stoichiometric, and the Zr terminated one is Zr rich. In order to make identical interface configurations at both ends of the ZrO₂ slab, the Ni slab with seven layers is employed for the T_0 structure, while the one with six layers is employed for T_1 . The resulting total numbers of atoms in the supercells range from 90 to 103, depending on the ZrO₂ termination and the translation states. In order to reveal intrinsic and fundamental bonding states at the incoherent interfaces, inclusion of yttrium and oxygen vacancies, which would be important for real Ni/YSZ systems, is not explicitly taken into account in the present study.

Spin-polarized electronic structure calculations of the interface system are performed using the Vienna Ab-Initio Simulation Package (VASP) program.¹⁹ The projector augmented wave method,^{20,21} which is an all-electron frozen-core-type method, is used to represent inner electrons, and electronic wave functions are expanded by plane waves up to a kinetic energy cutoff of 500 eV. The generalized gradient approximation (GGA) is used for the exchange-correlation potential, in which the GGA functional proposed by Perdew *et al.* is used.²² For the hexagonal-shaped interface super-

cells, Brillouin-zone (BZ) sampling is performed on a $4 \times 4 \times 1$ Monkhorst-Pack (MP) mesh centered at a Γ point (four irreducible k points).²³ Convergence tests using a $6 \times 6 \times 1$ MP mesh (seven irreducible k points) for the O terminated interfaces showed that differences in total energies and stresses of supercells are less than 1.6 meV/atom and 0.2 GPa, respectively. Works of separation (W_{sep}) for the interface cleavage, which are a measure of interface strength, are calculated from total-energy differences between the interface supercells and the individual Ni and ZrO_2 surface slabs with their fully relaxed atomic positions. It is found that the W_{sep} convergence for the denser k -point sampling ($6 \times 6 \times 1$ MP mesh) is less than 0.01 J/m². The above results ensure a good accuracy of the present supercell calculations to describe the interface structures and properties.

Excess energies γ of the interfaces are evaluated from total energies (E_T) of interface supercells and atomic chemical potentials (μ) for constituent atoms as follows.

$$\gamma = (E_T - n_{\text{Zr}}\mu_{\text{Zr}} - n_{\text{O}}\mu_{\text{O}} - n_{\text{Ni}}\mu_{\text{Ni}})/A. \quad (1)$$

In Eq. (1), A is an interface area, and n_i is the number of atoms i in the supercell. As will be shown later, ZrO_2 (111) surfaces are also calculated in this study, where a vacuum layer of 1.6 nm thickness is introduced in the supercell to obtain E_T for the surfaces. The values of μ_{Zr} , μ_{O} , and μ_{Ni} are constrained with equilibrium conditions of $\mu_{\text{ZrO}_2} = \mu_{\text{Zr}} + 2\mu_{\text{O}}$ and $\mu_{\text{Ni}} = \mu_{\text{Ni}(\text{bulk})}$, and thus μ_{O} ranges from $\mu_{\text{O}} = \mu_{\text{O}_2(\text{gas})}/2$ (oxidation limit) to $\mu_{\text{O}} = (\mu_{\text{ZrO}_2} - \mu_{\text{Zr}(\text{bulk})})/2$ (reduction limit). $\mu_{\text{O}_2(\text{gas})}$ and $\mu_{\text{Zr}(\text{bulk})}$ are obtained from total-energy calculations for O_2 molecule and hcp Zr metal.

To begin with, excess energies of ZrO_2 (111) surfaces and Ni/ ZrO_2 (111) interfaces are evaluated as a function of oxygen chemical potential, as shown in Fig. 2. It can be seen from Fig. 2(a) that the O terminated surface is most stable over the entire range of μ_{O} , and the Zr terminated surface exhibit a fairly high energy even in the reduction limit. This indicates that the clean ZrO_2 (111) surface always undergoes O termination, irrespective of oxygen chemical potentials. When the interface between ZrO_2 and Ni is formed [Fig. 2(b)], the O terminated structure is also more stable in higher μ_{O} , whereas the Zr terminated interface becomes more stable in the reduced condition of $\mu_{\text{O}} < -8.3$ eV. It is noted that the T_0 and T_1 structures for the two termination cases exhibit quite similar interface energies (an energy difference within 0.1 J/m²). It can be said that the interface termination is likely reversed from O to Zr termination under the reduced atmosphere, although the ZrO_2 (111) surface always has the O terminated structure. Both of the Zr and O terminated interfaces can be formed, depending on oxygen chemical potential. The similar situation was found in the previous theoretical study of the Nb/ Al_2O_3 system.⁶

The relaxed structures of the Zr and O terminated interfaces are depicted in Fig. 3, together with the interfacial W_{sep} values. For the Zr terminated interfaces, W_{sep} values are around 4.4 J/m², irrespective of the translation states, and are about 88% of W_{sep} (5.01 J/m²) for the Zr terminated nonstoichiometric Ni/ ZrO_2 (100) system calculated by Beltrán *et al.*⁸ The lattice misfit of the present interface (31%) is

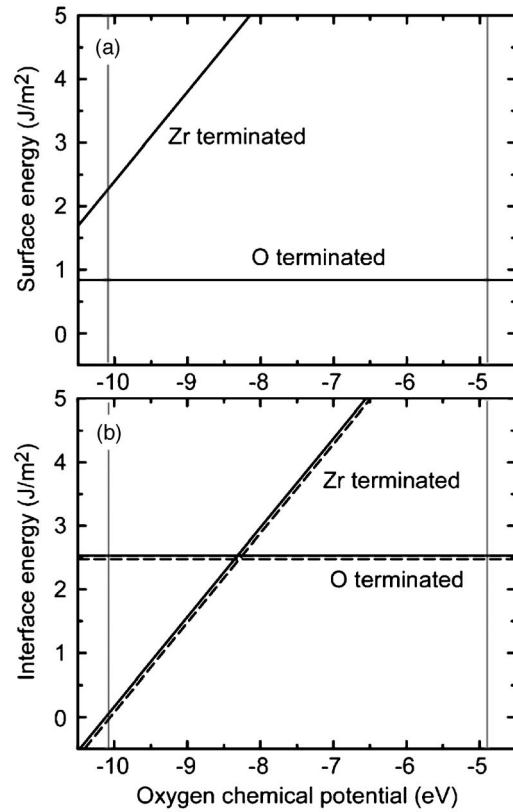


FIG. 2. Excess energies of (a) ZrO_2 (111) surfaces and (b) Ni/ ZrO_2 (111) interfaces as a function of oxygen chemical potential (μ_{O}). Vertical thin lines indicate μ_{O} values at the oxidation and reduction limits. In the plot of (b), solid lines denote energies for the T_0 -type Zr or O terminated interfaces, while broken lines indicate results for the T_1 -type interfaces (also see Fig. 1).

much larger than that of the Ni/ ZrO_2 (100) interface (less than 2%), and yet the W_{sep} values are not so much reduced as expected from the lattice-misfit difference.

In contrast, the O terminated (111) interfaces exhibit W_{sep} of about 0.5 J/m², which are much smaller than for the O terminated (100) interface ($W_{\text{sep}} = 5.74$ J/m²).⁸ This is mainly due to stoichiometry effects of the interfaces. In general, nonstoichiometric interfaces show larger W_{sep} than stoichiometric ones, due to considerable charge transfer occurring across interfaces.⁶ This is also the case for the present O terminated interface: the (100) system in Ref. 8 is O rich while the (111) system here stoichiometric. Therefore, it is not straightforward to make direct comparison of W_{sep} with Ref. 8, regarding the O terminated cases.

From Fig. 3, a number of structural characteristics in the incoherent interfaces can be observed. The Ni and Zr atoms (O atoms) in the first interface layers of the Zr terminated (O terminated) interfaces undergo large relaxations perpendicular to the interface planes. In particular, Ni atoms tend to rumple more considerably than Zr or O atoms, so that the Ni interface layers are not completely flat. In addition, bond lengths of Ni-Zr or Ni-O pairs across the interface are dependent on the Ni sites, which range from 0.24 nm to 0.30 nm for the Zr terminated interfaces, and from 0.19 nm to 0.30 nm for the O terminated ones. These results

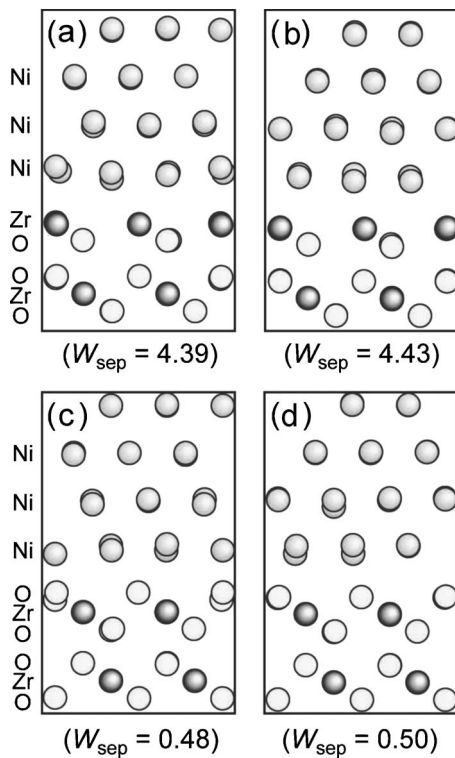


FIG. 3. Relaxed interface structures for Zr terminated and O terminated interfaces, viewed along the $[101]$ direction. (a) The Zr terminated interface in the T_0 translation state, and (b) the one in T_1 . In the similar way, the results for the T_0 and T_1 translation states for the O terminated case are drawn in (c) and (d), respectively. Works of separation W_{sep} (unit: J/m^2) are shown in the parentheses below the respective structures.

indicate that chemical environments of the Ni atoms in the interface layers are quite different, depending on the Ni sites on the ZrO_2 (111) surfaces.

In order to reveal electronic structures of the interfaces, atom-projected partial densities of states (PDOSs) are plotted in Fig. 4. For the Zr and O terminated interfaces having the T_0 -type structure, PDOS profiles for Ni, Zr, or O atoms at the center of each slab (denoted as “bulk”), interfacial Ni at the on-top site (Ni^a), interfacial Zr or O bonded to Ni^a are only shown. It is worth mentioning here that the PDOS shapes for the interfacial atoms in the two termination cases are different from those for the atoms in bulk, which indicates characteristic atomic interactions at the interfaces. In particular, the Ni-3d band is located around the band gap of ZrO_2 (E_g in Fig. 4), and then the metal-induced gap states (MIGSs) are observed in the PDOS profiles for interfacial Zr and O. The appearance of MIGSs is closely related to formation of the interfacial bonding.

Similarly to interfacial Zr or O, the PDOS shapes of the interfacial Ni atom are also different from that of bulk Ni. In the PDOS of bulk Ni, it can be seen that the majority-spin band (the upper panel) is located lower in energy than the minority-spin one (the lower panel), due to electron-exchange interactions. The resultant magnetic moment (MM) of bulk Ni is found to be $0.59\mu_B$ atom, and is in good agreement with the previous calculations for Ni.^{24,25} However, the

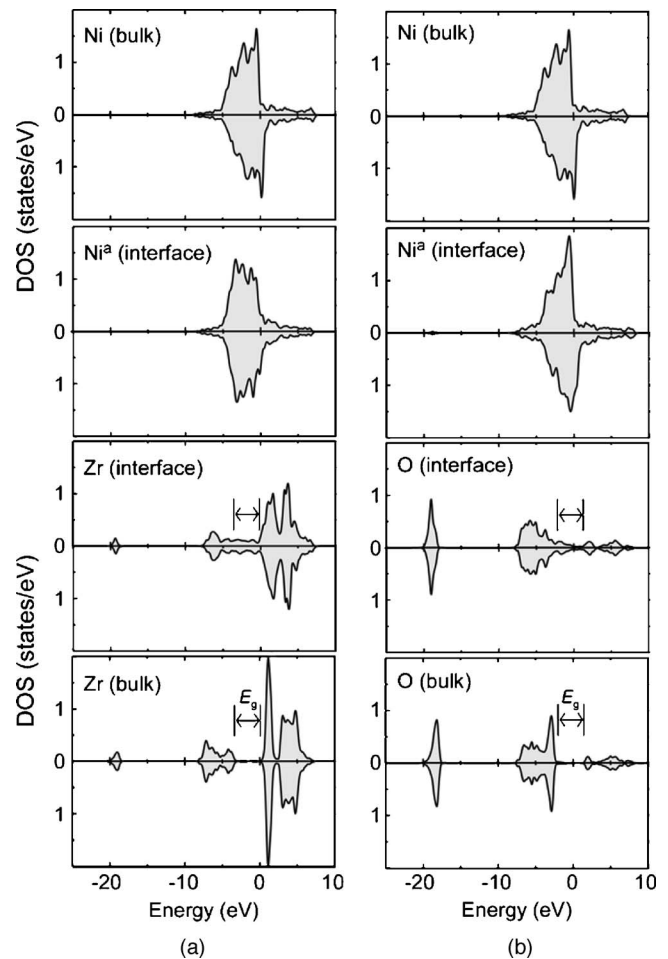


FIG. 4. Atom-projected DOS profiles for (a) the Zr terminated and (b) O terminated interface having the T_0 -type structure. In these plots, DOSs for atoms around the centers of Ni and ZrO_2 slabs (denoted as “bulk”), and those for interfacial Ni, Zr, and O in the on-top configuration are displayed. The Fermi level of each supercell is set at 0 eV.

degree of exchange splitting tends to decrease for Ni^a at the Zr terminated interface [Fig. 4(a)], and the calculated MM for Ni^a is found to be $0.19\mu_B$, which is quite smaller than that in bulk. This result is attributed with charge transfer from ZrO_2 to Ni. As stated before, the Zr terminated surface is Zr rich, and Zr is less electronegative than Ni. Therefore, considerable charge transfer from ZrO_2 to Ni can take place in the interface formation. The transferred electrons from ZrO_2 occupy the minority-spin orbital of Ni-3d originally unoccupied at the Fermi level, so that the Ni-3d orbitals are almost fulfilled by electrons and result in the similar DOS profiles between majority and minority spin, without exchange splitting. In contrast, the Ni^a PDOS at the O terminated interface does not change so significantly from that of bulk Ni, which is due to the fact that the O terminated ZrO_2 surface is stoichiometric, and thus significant charge transfer does not necessarily occur in the interface formation. It is noted, however, that the MM of Ni^a in the O terminated case is calculated to be $0.50\mu_B$, and is slightly smaller than that of bulk Ni.

PDOS curves for Ni at the different interfacial sites in the

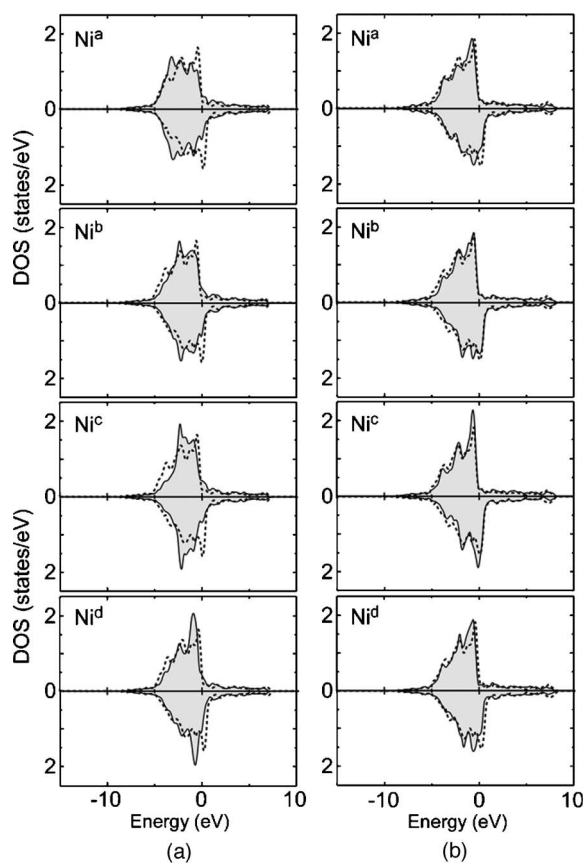


FIG. 5. DOS profiles for Ni atoms at different interfacial sites in (a) the Zr terminated and (b) the O terminated interface having the T_0 -type structure. Dotted curves overlaid on each figure correspond to DOS profiles of Ni at the center of the Ni slab. The Fermi level of each supercell is set at 0 eV.

Zr and O terminated T_0 -type structures are displayed in Fig. 5. In the case of Zr termination [Fig. 5(a)], it turns out that the PDOS profiles are varied depending on the Ni sites. The PDOS shape of Ni^a is quite different from that of bulk Ni, while the PDOS widths for other Ni atoms become narrower than those of Ni^a and bulk Ni. These features indicate different interactions of Ni-Zr at the interface. In the O terminated case [Fig. 5(b)], differences of interfacial Ni PDOSs from that of bulk Ni are not so large as in the Zr terminated case, but it is apparently observed that each PDOS of minority spin at around the Fermi level is changed in a different way depending on Ni sites. Such slight PDOS changes indicate that orbital polarization or overlap between Ni and O may occur even at the O terminated interface. From the above results, it can be said that Ni atoms in the interface layer of each interface system are in site-dependent chemical environments with underlying Zr or O atoms.

In order to investigate site-dependent bonding characteristics at the interfaces in more detail, electron-density (ED) differences in the T_0 -type interfaces are plotted in Fig. 6. Here, the EDs of the Ni and ZrO_2 slabs having the same atomic positions with the interface supercells are subtracted from those of the interfaces. Thus the contour maps indicate bond-formation behavior between Ni and ZrO_2 in the interface formation.

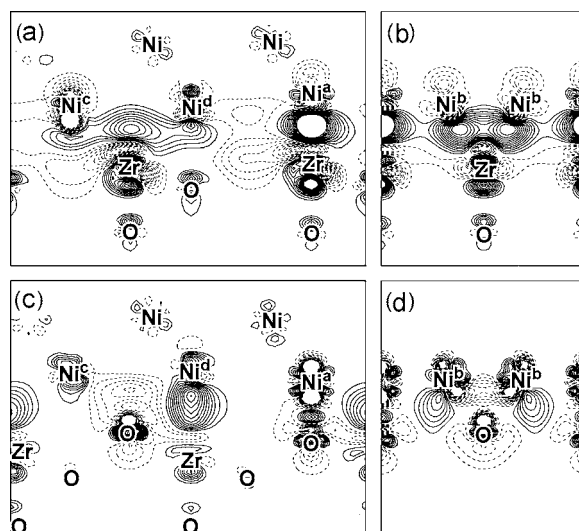


FIG. 6. ED difference maps for the T_0 structures of the Zr and O terminated interfaces. (a) and (c) are the plots on the $(01\bar{1})$ plane, while (b) and (d) are those on the $(\bar{2}11)$ plane. The contour lines are drawn from -0.12 to 0.12 with an interval of 0.01 in electrons/ \AA^2 , except for the zero contour line. Solid lines indicate positive values, while broken ones negative. On these cross sections, the on-top Ni (Ni^a), the two kinds of hollow-site Ni (Ni^c and Ni^d) and the asymmetric-site Ni (Ni^b) are present (also see Fig. 1).

In the Zr terminated case [Figs. 6(a) and 6(b)], it is obvious that the large areas with positive ED differences are present at the interface. This is due to that considerable charge transfer from Zr to Ni occurs and the electrons are sheared between atoms at the interface layers. Such features can also be understood from the DOS profiles shown in Fig. 5. As is seen in Fig. 6(a), the ED significantly increases between the on-top Ni atom (Ni^a) and Zr, and the increased region is rather localized between the two atoms, which indicates their strong covalent interaction. The strong covalency of Ni^a -Zr can also be understood from its bond length (0.242 nm), which is much smaller than the sum of their atomic radii (0.285 nm).²⁶ Around the hollow-site Ni^c and Ni^d atoms, the increase in ED is observed as well, but the electrons mainly concentrate above Zr. Therefore, the positively charged Zr atom no longer has direct interactions with Ni^c and Ni^d , but interacts with the electrons accumulated around the Ni interstitial region in an electrostatic (ionic) manner. Regarding the asymmetric-site Ni atoms [Ni^b in Fig. 6(b)], the ED increases at around the midpoint with Zr, and also the increased region is shared among the two neighboring Ni atoms. This indicates that the Ni-Zr bonds can be described by covalent interactions with partial metallic characters. As shown above, the chemical interactions across the Zr terminated interface exhibit a site-dependent feature from ionic through covalent/metallic characters of bonding.

The increased ED regions at the O terminated interface [Figs. 6(c) and 6(d)] are much smaller than those in the Zr terminated case, since the O terminated ZrO_2 surface is stoichiometric and thus large charge transfer does not necessarily take place. In such a case, ED redistribution in the Ni layers may occur due to the electrostatic field of the ionic

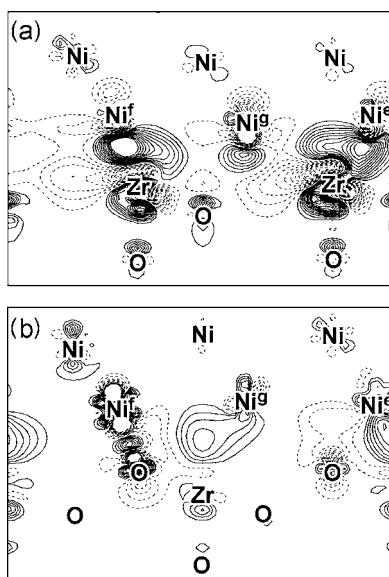


FIG. 7. ED difference maps on the $(01\bar{1})$ planes for the T_1 structures of the Zr terminated (a) and O terminated (b) interfaces. The contour maps are drawn in the similar manner with Fig. 3.

ZrO₂ layers, and the bonding of the O terminated interface may arise from image-chargelike interactions between Ni and ZrO₂.^{1,2} Obviously, the EDs of the Niⁱ-Ni^j interstitial regions decrease (positively charged), while the EDs just above Zr in the second ZrO₂ layer increase (negatively charged). Such decrease and increase in ED can induce attractive ionic interactions with the oppositely charged O and Zr atoms, respectively. However, it is worth mentioning here that the on-top Ni^a-O pair exhibits an increased ED region localized between the two atoms, indicating the covalent interaction. Therefore, charge rearrangement in the Ni layer does not always result in ionic interactions with ZrO₂, but sometimes gives rise to interfacial covalent bonds depending on the bonding-pair configurations. This can be attributed to the fact that Ni-3*d* orbitals originally have an electron-unoccupied state, as stated in Figs. 4 and 5. The on-top Ni^a-O configuration has a smaller bond length (0.197 nm) than the others (more than 0.21 nm), and the Ni-3*d* orbitals atop O are subject to large polarization due to the negatively charged O atom [see Fig. 6(c)]. Although such detailed interactions of Ni^a-O cannot easily be resolved only from the PDOS profiles shown in Fig. 5, the orbital hybridization of Ni-3*d* with O-2*p* occurs, which results in formation of the covalent Ni^a-O bond. It can be said that the O terminated interface also exhibits a multiplicity of chemical bonds with site dependency, as a result of the ED redistribution and orbital polarization across the interface.

The feature of multiple bonding characters found for the T_0 structures is also applicable to the T_1 translation state. Figure 7 shows ED-difference maps for the T_1 -type Zr and O terminated interfaces. In the Zr terminated case [Fig. 7(a)], the Ni atoms located at the sites slightly off from the exact on-top location (Ni^e and Ni^f) tend to form covalent bonds with Zr. It is noted that the Ni^f-Zr and Ni^e-Zr bond lengths of 0.248 nm and 0.257 nm are close to the covalently bonded on-top Ni^a-Zr (0.242 nm) and asymmetric Ni^b-Zr

(0.256 nm) lengths in the T_0 structure (see Fig. 6), respectively. Moreover, the electron-accumulated region manifests itself between Ni^e and Ni^s, which contributes to ionic interactions with the Zr cation below. In the O terminated interface [Fig. 7(b)], the Ni^f-O pair forms a covalent bond, and its bond length of 0.198 nm is quite similar to that of on-top Ni^a-O (0.197 nm) in the T_0 translation state [see Fig. 6(a)]. Ni-O pairs with larger bond lengths [Ni^e-O and Ni^s-O in Fig. 7(b)] no longer have covalent interactions. Alternatively, the increases in ED above Zr in the second layer, inducing their image-chargelike ionic interactions, can be observed. Even in the translated state, therefore, multiple chemical bonds ranging from ionic to covalent are realized in accordance with their local atomic configurations. It is noted, however, that the magnitudes of image charges induced at the interface are smaller than those in the T_0 -type structure [see Fig. 6(c)]. The individual image charges induced are sensitive to the translation state.

It should be noted here that the similar W_{sep} values in the two translation states for both the Zr and O terminations (shown in Fig. 3) should originate from the multiplicity of the interface bonding. If interface-energy differences among translation states are rather large, the energy penalty would be compensated by generation of misfit dislocations. For instance, the previous calculations of coherent-model MgO/Ag(001) interfaces, which are in reality semicoherent with a lattice misfit of about 3%, yielded a large energy difference of about 0.4 J/m² between different translation states.³ As compared to that, the changes in W_{sep} due to the relative translations are much smaller in the present case (less than 0.04 J/m²). Since the real incoherent interface structure can be represented by a mixture of the different translation states, the invariability of interface energy against the relative translation states may explain why the interface structures without long-range lattice continuity can be formed as a stable structure.

W_{sep} values mean mechanical energy release upon interface fracture, and are used as a good measure of interface strength. In the case of coherent interfaces, W_{sep} values correspond to the energy required to break interfacial bonds in a particular configuration. However, incoherent interfaces contain a multiplicity of interfacial bonds, and thus the situation upon interfacial fracture is more complicated, although the W_{sep} values in Fig. 3 are independent of the translation states. In particular, energies to break chemical bonds at incoherent interfaces are also dependent on the individual bond characters, which should affect the mechanical response to applied stresses. In order to reveal an effect of the multiple interfacial bonding on mechanical properties of incoherent interfaces, first-principles tensile tests are performed for the incoherent Ni/ZrO₂(111) interfaces.

In the present first-principles tensile tests, uniaxial tensile strains are imposed onto the stable interface structures. The supercell edge lengths normal to the interfaces (the [111] direction) are elongated in small increments, and all atomic positions are relaxed at each strained states. The supercell edge lengths parallel to the interfaces (the $[\bar{1}01]$ and $[\bar{1}10]$ directions) are fixed throughout the tensile tests, preventing Poisson contraction, in order to reduce computational time.

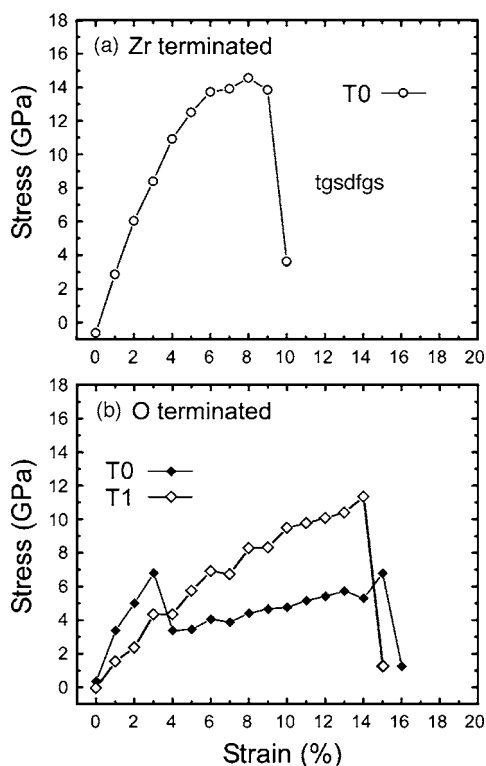


FIG. 8. The stress-strain curves for the Zr terminated and O terminated interfaces. The T_0 structure of the Zr terminated interface showed cleavage fracture inside ZrO_2 . In (a), the profile of T_0 is only displayed, but it is expected that the T_1 -type structure shows the similar curve, since that translation state also have a rather large W_{sep} value, resulting in cleavage inside ZrO_2 . In contrast, the O terminated interfaces exhibited fracture at the interface planes. However, it is interesting to point out the different stress-strain behaviors between the two translation states.

Strictly speaking, therefore, the present tensile tests correspond to uniaxial extension. Poisson contraction may decrease theoretical tensile stresses of bulk and grain boundaries, and thus maximum stresses for fracture without Poisson contraction are regarded as upper bounds of tensile strength of the incoherent interfaces.^{27,28}

Figure 8 displays stress-strain curves of the Ni/ ZrO_2 (111) interfaces. For the T_0 -type Zr terminated interface [Fig. 8(a)], the stresses readily increase with rising strains, reach a maximum stress of 14.5 GPa at the 8% strain, and abruptly drop at a strain of 10%. In this case, the interface itself does not undergo fracture, and cleavage between O planes in the second and third ZrO_2 layers from the interface plane actually takes place. It can be said that this stress-strain profile reflects typical brittle fracture behavior inside ZrO_2 . In fact, the W_{sep} value for cleavage between (111) O planes in ZrO_2 is found to be 1.69 J/m^2 ($=2\gamma_s$, γ_s is the surface energy), and is much smaller than those for cleavage between Ni(111) layers (4.08 J/m^2) and at the interface (4.39 J/m^2), which are obtained by calculations of separate Ni and ZrO_2 surface slabs. In addition, it can be seen from interfacial bond-length changes against strains in Fig. 9(a) that the bond lengths across the interface do not exhibit notable changes against strains. Thus the interface bonding of the Zr terminated case

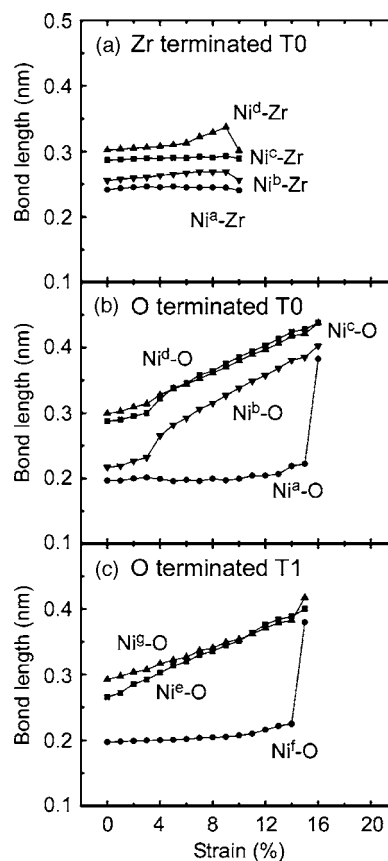


FIG. 9. The bond-length changes as a function of tensile strain. It is noted that the T_0 -type interfaces contain four kinds of bonding-pair configurations, whereas in the case of the T_1 -type O terminated interface, three kinds of Ni-O configurations with different bond lengths are present (also see Fig. 1).

is rather rigid against tensile loading. As shown in Fig. 3, the Zr terminated interface in the different translated state of T_1 exhibit the similar W_{sep} value, and it can be expected that cleavage inside ZrO_2 occurs, showing the quite similar stress-strain profile to Fig. 8(a).

In contrast, by the tensile tests of the O terminated interfaces, cleavage at the interface planes is observed, as expected from their small W_{sep} values of around 0.5 J/m^2 , whereas the stress-strain curves show different behavior from that of the Zr terminated case. In the case of the T_0 structure, the stresses increase almost linearly with strains up to 3%, showing a maximum stress of 6.8 GPa, and yet decrease at the 4% strain. Subsequently, the stresses again gradually increase with increasing strains, and overall fracture throughout the interface plane eventually occurs at the 16% strain.

Such a stress-strain behavior of the T_0 -type O terminated interface is attributed to different strength of individual chemical bonds across the interface. It can be seen from the bond-length changes [Fig. 9(b)] that Ni-O bonds in the hollow and asymmetric configurations (Ni^b -O, Ni^c -O, and Ni^d -O) exhibit jumps in their bond-length profiles at the 4% strain, and thereafter their bond lengths readily increase with strains. This indicates that these Ni-O bonds start to break at a strain of 4%, and no longer contribute to the interface

adhesion for the further tensile strains. However, the Ni^a-O bond maintains its length around 0.2 nm until the 15% strain, and the bond length rapidly increases at a strain of 16%, meaning complete fracture of the interface. Therefore, the bonding strength of Ni-O in the on-top configuration, which has a covalent character shown in Fig. 6(c), is rather large as compared to those in the other configurations. Such a site-dependent bonding feature over the interface results in the distinct stress-strain profile of the T₀-type O terminated interface.

The T₁-type O terminated interface also exhibits a different stress-strain profile from the T₀-type one [Fig. 8(b)]. Considerable stress reduction during strain loading, as found in the T₀-type O terminated interface, is not observed in this case, but the profile for T₁ is not as smooth as that in the Zr terminated case. This is due to bond-breaking processes at the interfaces, beginning from the onset of strain loading. As can be seen in Fig. 9(c), the Ni^e-O and Ni^g-O pairs increase their distances monotonically with strains, which indicates that these Ni-O bonds are broken successively with strain. In contrast, the Ni^f-O bond maintains its length of about 0.2 nm even for larger strains. In Fig. 7(b), the Ni^f-O pair exhibits strong covalency, and thus the presence of the covalent bonds across the incoherent interface is responsible for the interface strength. In the T₁-type interface, three covalent Ni^f-O pairs are present per unit [see Fig. 1(b)], which results in the larger maximum stress of about 11 GPa, as compared to that of the T₀-type interface (6.8 GPa) with one covalent Ni^a-O bond (on-top configuration) in the repeat unit. Owing to the on-top covalent pairs and their numbers contained in the translation states, the real incoherent O terminated interfaces do not undergo homogeneous cleavage over the interface plane. The fracture behavior is very sensitive to the

translation states and their associated site-dependent interfacial bonding multiplicity.

In this paper, the first-principles results of the Ni/ZrO₂(111) interfaces are reported, in order to reveal a bonding nature of incoherent metal/oxide interfaces. Even though the interface bonding is composed of one type of atomic-species pairs such as Ni-Zr or Ni-O, depending on the interface termination, the interfacial atomic pairs exhibit site-dependent bonding characters. The bonding pair in the on-top configuration tends to have the strong covalent bond, while other Ni atoms in the hollow and other configurations form metallic or ionic for Zr termination, or ionic bonds for O termination. As compared to the covalent bond in the on-top configuration, such metallic or ionic interfacial interactions are neither directional nor rigid, which may stabilize the elongated or distorted bonding configurations intrinsically contained in the incoherent interfaces. Such a multiplicity of interfacial bonds also result in interface energetics independent of the translation states, but strongly affect the atomic-scale cleavage behavior of the incoherent interfaces. The bonding multiplicity cannot be understood by the image charge theory and previous coherent-model calculations, and must be new findings to depict general incoherent interfaces. This idea will thus be applicable to any heterointerface system as a generic bonding picture for large-mismatched interfaces.

This work was performed as a part of the Nanostructure Coating Project carried out by New Energy and Industrial Technology Development Organization. This work was also partly supported by a Grant-in-Aid for Scientific Research from the Ministry of Education, Sports, Science and Culture of Japan. K.M. also acknowledges useful advice by M. Kohyama at AIST, Japan, regarding computation of metal/oxide interfaces.

*Corresponding author. Electronic address: k.matsunaga@materials.mbox.media.kyoto-u.ac.jp

¹M. W. Finnis, *J. Phys.: Condens. Matter* **8**, 5811 (1996).

²F. Ernst, *Mater. Sci. Eng., R.* **14**, 97 (1995).

³T. Hong, J. R. Smith, and D. J. Srolovitz, *Acta Metall. Mater.* **43**, 2721 (1995).

⁴G. L. Zhao, J. R. Smith, J. Reynolds, and D. J. Srolovitz, *Interface Sci.* **3**, 289 (1996).

⁵I. G. Batirev, A. Alavi, M. W. Finnis, and T. Deutsch, *Phys. Rev. Lett.* **82**, 1510 (1999).

⁶W. Zhang and J. R. Smith, *Phys. Rev. B* **61**, 16883 (2000).

⁷A. Christensen and E. A. Carter, *J. Chem. Phys.* **114**, 5816 (2001).

⁸J. I. Beltrán, S. Gallego, J. Cerdá, J. S. Moya, and M. C. Munoz, *Phys. Rev. B* **68**, 075401 (2003).

⁹R. Benedek, A. Alavi, D. N. Seidman, L. H. Yang, D. A. Muller, and C. Woodward, *Phys. Rev. Lett.* **84**, 3362 (2000).

¹⁰A. P. Sutton and R. W. Balluffi, *Interfaces in Crystalline Solids* (Oxford University Press, New York, 1996).

¹¹Y. Ikuhara and P. Pirouz, *Microsc. Res. Tech.* **40**, 206 (1998).

¹²G. Dehm, M. Rühle, G. Ding, and R. Raj, *Philos. Mag. B* **71**, 1111 (1995).

¹³C. Scheu, W. Stein, and M. Rühle, *Philos. Mag. A* **78**, 439 (1998).

¹⁴T. Sasaki, K. Matsunaga, H. Ohta, H. Hosono, T. Yamamoto, and Y. Ikuhara, *Sci. Technol. Adv. Mater.* **4**, 575 (2003).

¹⁵T. Sasaki, K. Matsunaga, H. Ohta, H. Hosono, T. Yamamoto, and Y. Ikuhara, *Mater. Trans., JIM* **45**, 2137 (2004).

¹⁶J. H. Van Der Merwe, *J. Appl. Phys.* **34**, 117 (1963).

¹⁷Y. Ikuhara, P. Pirouz, A. H. Heuer, S. Yadavalli, and C. P. Flynn, *Philos. Mag. A* **70**, 75 (1994).

¹⁸J. W. Matthews, *Dislocations in Solids*, edited by F. R. N. Nabarro, Vol. 2 (North-Holland Publishing, Amsterdam, 1979).

¹⁹G. Kresse and J. Furthmüller, *Comput. Mater. Sci.* **6**, 15 (1996).

²⁰P. E. Blöchl, *Phys. Rev. B* **50**, 17953 (1994).

²¹G. Kresse and D. Joubert, *Phys. Rev. B* **59**, 1758 (1999).

²²J. P. Perdew, J. A. Chevary, S. H. Vosko, K. A. Jackson, M. R. Pederson, D. J. Singh, and C. Fiolhais, *Phys. Rev. B* **46**, 6671 (1992).

²³H. J. Monkhorst and J. D. Pack, *Phys. Rev. B* **13**, 5188 (1976).

²⁴J. H. Cho and M. H. Kang, *Phys. Rev. B* **52**, 9159 (1995).

²⁵E. G. Moroni, G. Kresse, J. Hafner, and J. Furthmüller, *Phys. Rev. B* **56**, 15629 (1997).

²⁶C. Kittel, *Introduction to Solid State Physics*, 6th ed. (John Wiley & Son, Inc., New York, 1986).

²⁷M. Kohyama, *Philos. Mag. Lett.* **79**, 659 (1999).

²⁸G. H. Lu, S. Deng, T. Wang, M. Kohyama, and R. Yamamoto, *Phys. Rev. B* **69**, 134106 (2004).